

53613

**The estimation of surface latent heat flux  
over the ocean and its relationship to Marine Atmospheric Boundary Layer  
(MABL) structure**

Stephen P. Palm<sup>\*a</sup>

Geary K. Schwemmer<sup>b</sup>

Doug Vandemark<sup>c</sup>

Keith Evans<sup>d</sup>,

David O. Miller<sup>a</sup>

Belay B. Demoz<sup>d</sup>

<sup>a</sup>Science Systems and Applications Inc., Lanham, MD

<sup>b</sup>Laboratory for Atmospheres  
NASA/Goddard Space Flight Center  
Greenbelt, MD

<sup>c</sup>Laboratory for Hydrospheric Processes  
NASA/Goddard Space Flight Center  
Wallops Isl., VA

<sup>d</sup>Joint Center for Environmental Technology  
University of Maryland Baltimore County  
Baltimore, MD

Boundary Layer Meteorology  
July, 2001

---

\* Correspondence: Email: [spp@virl.gsfc.nasa.gov](mailto:spp@virl.gsfc.nasa.gov); WWW: <http://bll.gsfc.nasa.gov>; Phone: 301-614-6276; Fax: 301-614-5492

## ABSTRACT

A new technique combining active and passive remote sensing instruments for the estimation of surface latent heat flux over the ocean is presented. This synergistic method utilizes aerosol lidar backscatter data, multi-channel infrared radiometer data and microwave scatterometer data acquired onboard the NASA P-3B research aircraft during an extended field campaign over the Atlantic ocean in support of the Lidar In-space Technology Experiment (LITE) in September of 1994. The 10 meter wind speed derived from scatterometers and lidar-radiometer inferred near-surface moisture are used to obtain an estimate of the surface flux of moisture via a bulk aerodynamic formula. The results are compared with the Special Sensor Microwave Imager (SSM/I) daily average latent heat flux and show reasonable agreement. However, the SSM/I values are biased low by about  $15 \text{ W/m}^2$ . In addition, the Marine Atmospheric Boundary Layer (MABL) height, entrainment zone thickness and integrated lidar backscatter intensity are computed from the lidar data and compared with the magnitude of the surface fluxes. The results show that the surface latent heat flux is most strongly correlated with entrainment zone depth, MABL height and the integrated MABL lidar backscatter, with corresponding correlation coefficients of 0.39, 0.43 and 0.71, respectively.

**Keywords:** backscatter, boundary layer height, entrainment zone, latent heat flux, lidar

## Popular Summary

**The oceans** absorb a considerable fraction of the sunlight reaching the surface of the **Earth**. The energy in this sunlight is stored as heat and is later transferred to the **atmosphere** by either conduction via direct contact (sensible heat), radiated as infrared **light**, or by evaporating water at the surface thereby increasing the humidity of the **overlying air**. The energy used to evaporate the water does not immediately raise the air **temperature**, but is stored in the water vapor and known as latent heat. It is released into **the air as sensible heat** when the water vapor condenses into cloud droplets. Over much **of the ocean**, the amount of energy transferred to the atmosphere by evaporation greatly **exceeds** the amount of heat transferred by radiation or sensible heat exchange. The latent **heat released** by condensation is a primary driving force of atmospheric circulation and **tropical storm** formation. It is well known that tropical storms and hurricanes derive their **energy** from the transfer of sensible and latent heat from warm ocean waters to the air. Though very important to climate and weather forecasting, the production of water vapor **over the ocean** is very difficult to measure remotely (from earth orbit). To date, the only **instrument** capable of this is the Special Sensor Microwave Imager (SSM/I). In this paper **we present** an alternate method based on the synergistic use of data from several **instruments**, which are or will soon be in orbit. Combining the data from these **instruments** using our new technique will provide climate and weather forecasters with a **powerful new tool** for observing the rate of energy exchange between the ocean and the **atmosphere**. It will provide more global coverage, higher accuracy, and higher spatial **resolution** than the current instrument.



## 1. Introduction

The flux of water vapor over the global oceans has important implications for a wide range of geophysical processes. Due to the low albedo of the seas and their large extent, the global oceans absorb a considerable fraction of the solar radiation reaching the surface of the Earth. This energy is stored as heat and is subsequently transferred to the atmosphere by processes such as convection, radiation and evaporation. Over much of the ocean, the amount of energy transferred by evaporation greatly exceeds that by radiation or sensible heat exchange. The subsequent latent heat released by condensation is a primary driving force of atmospheric circulation and tropical storm formation. The surface energy flux can also greatly enhance the early development and intensification of mid-latitude cyclones off the east coast of the US, according to Kuo et al. (1991) and Atlas (1987). It is well known that tropical storms and hurricanes derive their energy from the flux of sensible and especially latent heat over warm ocean waters. The flux of water vapor from the sea has a large influence on sea surface temperature and is needed to couple atmospheric and oceanic circulation models that are used to forecast weather and climate (Zhang and McPhaden, 1995). In addition, air-sea interaction plays a major role in the El Nino-Southern Oscillation (ENSO) and the 50 day oscillation as well as in the initiation and maintenance of heat waves, droughts and other anomalies (Atlas et al., 1996).

Until very recently, it has been impossible to accurately monitor latent heat flux over the ocean because of the scarcity of data. With the advent of orbiting remote sensing instruments such as the Special Sensor Microwave/Imager (SSM/I), Advanced Very High Resolution Radiometer (AVHRR) and the European Remote Sensing Satellite (ERS-1), the capability now exists to routinely estimate the fluxes of heat, moisture and momentum over the global oceans (Liu, 1988; Chou et al, 1995). Schulz and Jost (2000) have produced a global oceanic data set of latent and sensible heat fluxes from SSM/I data from 1987 to present. Chou et al (2001) have generated a similar data set spanning 1987 to 1994. These works represent giant leaps in our ability to globally map the distribution of near-surface water vapor and surface fluxes for process studies and climate monitoring. At present, the only method available to produce global energy fluxes are those pioneered by Liu and others that use the SSM/I measured microwave radiances. In this paper we explore a potential technique to retrieve water vapor flux over the ocean using a combination of airborne lidar, microwave scatterometer and infrared radiometer data that may someday provide global surface moisture flux estimates from orbiting lidar systems such as the Geoscience Laser Altimeter System (GLAS), which is scheduled to launch in December, 2001 (Spinhirne and Palm, 1996), and the 2004 PICASSO (Path finder Instruments for Cloud and Aerosol Observations) mission (Winker and Wielicki, 1999).

In addition to presenting the flux retrieval technique, we will use the lidar data to obtain information on the height and structure of the Marine Atmospheric Boundary Layer (MABL) and investigate the possible correlation between the surface latent heat flux and the MABL structure. Section 2 will describe the instrumentation and measurements which are used in section 3 to derive the latent heat flux. Section 4 presents a correlation analysis between lidar derived MABL parameters and the latent flux, with summary and conclusions given in section 5.

## 2. Measurements

Airborne atmospheric backscatter lidar measurements were made in conjunction with scanning radar measurements of surface winds, and infrared radiometer sea surface temperature measurements while participating in the Lidar In-space Technology Experiment (LITE) airborne correlative measurements program, September 11 through September 19, 1994 (McCormick, 1996). LITE, which was flown aboard the space shuttle Discovery, was the first atmospheric lidar to operate from space. As part of the LITE airborne correlative measurements program, the NASA P-3B was outfitted with numerous instruments and flight lines were laid out to correlate with specific overpasses of the shuttle, according to figure 1. All of the flights were over the open Atlantic Ocean with a few tracks nearing the coasts of South America and Africa. All 5 tracks were made during the nighttime hours. A description of the instrumentation flown aboard the NASA P-3B is presented below.

## **2.1 Instrumentation**

### **2.1.1 LASAL**

Atmospheric backscatter profiles were acquired by the Large Aperture Scanning Airborne Lidar (LASAL), (Palm et al., 1994). LASAL is an elastic backscatter lidar with a 450 mJ, 50 Hz Nd:YAG laser transmitter and a 55 cm aperture telescope in conjunction with a full aperture scan mirror to measure atmospheric aerosol and cloud backscatter in 3 dimensions, and is particularly suited for the study of the Planetary Boundary Layer (PBL). Mounted in the bomb bay of NASA's P-3B research aircraft, it is capable of cross-track scanning  $\pm 45^\circ$  at scan rates up to  $90^\circ$  per second. The laser, data system and real-time display are housed in the passenger section of the aircraft. Measurements are made of relative attenuated aerosol backscatter from the height of the plane to the surface. During the LITE flights, LASAL was operated in across-track scanning mode (9/11 and 9/17) and in nadir-only pointing mode (9/13, 9/15 and 9/19). Algorithms have been designed to retrieve the PBL height and entrainment zone depth from the backscattered return, as well as visualize the structure and organization of convection within the planetary boundary layer (PBL). Details of the technique used to derive PBL height from lidar backscatter signals can be found in Palm et al (1998) and Melfi et al (1985). Further methods have been developed to estimate the lifting condensation level from the cloud base height derived from the lidar backscatter data. Combining these data with the SST we can calculate the near-surface mixing ratio, which is a crucial component of the surface moisture flux. A description of the near-surface moisture retrieval technique and an example of recent results are presented in section 2.2.

### **2.1.2 ROWS**

The Radar Ocean Wave Spectrometer (ROWS) is a conical scanning Ku-band radar that records directional long and short wave information, from which are derived 10 meter wind vectors (Vandemark et al., 1994). ROWS is an azimuth scanning radar system designed to support satellite remote sensing with active microwave sensors. The system provides a field-tested method for estimating surface wind speed and 2-D ocean long wave spectra with the extensive spatial coverage unique to an aircraft sensor. ROWS has participated in numerous air/sea interaction field experiments including MASEX (Mesoscale Air Sea interaction Experiment), SIR-B, FASINEX (Frontal Air Sea Interaction Experiment), LEWEX, SWADE, the ERS-1 SAR Wave experiment, and LITE. Research topics addressed using airborne ROWS data include the retrieval of directional long-wave spectra (DWS) from both airborne and satellite platforms, the integration of long wave spectral estimates into air/sea interaction models, and the study of surface wind speed retrieval algorithms. Operationally, ROWS switches at a constant rate between an off-nadir 'spectrometer-mode' antenna and a nadir pointing 'altimeter-mode'. The two modes

allow simultaneous measurement of altimeter data along with the long wave information. The ROWS data products available for a given flight leg are:

- a) directional long wave spectra
- b) relative radar cross-section (RCS) versus azimuth versus 10-180 elevation
- c) altimeter-derived RCS versus 0-120 elevation (nondirectional in azimuth)
- d) altimeter-derived sea surface significant wave height (SWH)
- e) estimation of surface wind speed from altimeter-derived mean-square-slope

The nominal along-track spacing of the above data products is 20 km for a and 2 km for b-e.

### **2.1.3 University of Massachusetts CSCAT and KUSCAT**

CSCAT and KUSCAT are vertically polarized pencil beam airborne scatterometers at C-band and Ku-band, respectively, which were developed by the Microwave Remote Sensing Laboratory (MIRSL) at the University of Massachusetts with support of NASA over the last decade. These scatterometers provide a field-tested method for measuring the full azimuthal normalized radar cross section (NRCS) of the ocean surface. From the NRCS measurement the near surface wind vector can be estimated. These instruments have participated in several field campaigns, the most recent ones being Tropical Ocean Global Atmosphere Couple Ocean-Atmosphere Response Experiment (TOGA COARE), LITE, and Hurricane Tina.

Both instruments utilize microstrip-phased arrays to frequency scan their pencil beam from 20 degrees to 50 degrees incidence. These antennas are a frequency scaled version of each other, and therefore their patterns are almost identical. A central VXI-based data acquisition/digital control unit has been designed by MIRSL to run one or both instruments simultaneously. During operation, the antennas are rotated in azimuth at 120 rpm and the incidence angle of each scatterometer is switched sequentially between the four incidence angles at a pulse repetition frequency that results in the maximum number of independent data samples, at all four incidence angles simultaneously, as the aircraft is following its flight line. Hence, the system can provide the full azimuthal NRCS response at two frequencies and four incidence angles (20, 30, 40 and 50 degrees) every 1/2 second. Using the SASSII and CMOD4 models the near surface wind vector can be estimated from the NRCS response. Statistically stable averages are available every sixteen seconds. MIRSL data products available for a given flight leg are:

- a) Simultaneous C- and Ku-band full-azimuthal normalized radar cross section (NRCS) measurements at 4 incidence angles
- b) Near surface wind vector estimates with an eight level redundancy

### **2.1.4 Sea Surface Temperature**

The NASA/JPL Sea Surface Temperature Radiometer (SSTR) is a multispectral, infrared radiometer which operates in the down-looking mode. The radiometer, whose calibration characteristics are described elsewhere (Hagan 1988), is a six-channel, filter-wheel radiometer with a field of view of 1 mrad and a collecting aperture of 20 cm. Modulated radiance is focused by a Cassegrain telescope on to a liquid nitrogen-cooled HgCdTe detector. Interference filters define the optical bandpasses: two spectral regions approximately 80 wavenumbers wide and centered at  $860\text{ cm}^{-1}$  and  $940\text{ cm}^{-1}$ , and four contiguous spectral regions between 40 and 50 wavenumbers wide which cover the interval between 825

$\text{cm}^{-1}$  and  $1005 \text{ cm}^{-1}$ . The two wide bandpasses nearly match the 11 and 12 micron channels used by the Advanced Very High Resolution Radiometer (AVHRR), and the four more narrow bandpasses further subdivide the window region. The precision of the radiometer is 0.006 Celsius for data acquired at 1 Hz, and the absolute calibration accuracy of the instrument is 0.07 Celsius. The radiometer views the ocean through a germanium window, whose temperature was monitored by internal and external platinum resistance temperature (PRT) sensors accurate to 0.01 Celsius. The PRT readings are used to correct the detected radiance for the contribution by the window emission.

Sea surface temperature estimates are derived by regression of the brightness temperature measurements obtained in the four narrow optical bands. The technique is an extension of the method of Prabhakara et al. (1974). The regression relations, which differ for tropical and subtropical regions, were determined empirically from an extensive series of SSTR observations obtained during recent climate experiments such as TOGA COARE and the Central Equatorial Pacific Experiment (CEPEX). High accuracy in situ water vapor measurements were obtained simultaneously with the SSTR radiance profiles, and the effects of water vapor on the accuracy of SST retrievals are discussed in Hagan and Rogers (1997). A similar regression approach for deriving water vapor content is being developed following the method of Dalu (1986). Derived SST accuracy is on the order of  $0.2 \text{ }^\circ\text{C}$ .

The SSTR measurements were used to provide an estimate of the 10 meter air temperature for the retrieval of near-surface moisture as discussed in section 2.2.2. They are also used to calculate the surface saturation mixing ratio for use in latent heat flux calculation (see section 3). The SSTR data were unfortunately not available at all locations due to either the presence of clouds or data recording problems. In these areas, NOAA weekly average SST values were used instead. We checked the level of agreement between the SSTR retrieved values and the NOAA data for the same areas and found that they matched fairly well. Figure 2 is a plot of the SSTR retrieved SST values versus the NOAA data for the 16 dropsonde locations shown in figure 1. The data show good agreement, but the NOAA measurements appear to be a little warmer than the SSTR values for temperatures above about 24 Celsius. However, it must be kept in mind that we are comparing a weekly average value (NOAA data) with an instantaneous provided by the SSTR.

### **2.1.5 National Center for Atmospheric Research (NCAR) Dropsondes**

The NASA P-3B carried a total of 25 Lightweight Omega Digital Dropwindsondes (LOD2) for use during the LITE under flights. The LOD2 measures wind speed and direction, temperature, relative humidity and pressure as it falls to the surface on a parachute at an average speed of about 8 m/s (Hock and Cole, 1991). The data are radioed back to the aircraft at a rate of 4 Hz and stored on hard disk for future analysis. This gives a vertical resolution of the thermodynamic data of about 2 meters. The resolution of the wind speed and direction is much less (about 200 meters) because vertical averaging of the sonde position data is necessary to derive the wind vectors. The profiles are displayed in real time using a laptop PC as they are acquired. During a typical flight, the dropsondes were released at approximately two hour intervals and are indicated by the '+' signs in figure 1. These data were used to compare and validate the LASAL-SSTR retrievals of 10 meter moisture. A more detailed description of the dropsondes can be found in Palm et al. (1998).

## **2.2 LASAL Derived Measurements**

### 2.2.1 Near surface moisture

A technique was developed by Palm et al. (1998) to retrieve near-surface moisture over the ocean using a combination of lidar backscatter data and radiometric SST data. The method uses the statistical distribution of boundary layer cloud top height in a 50 km long segment to estimate the cloud base height. The cloud top height is obtained directly from the lidar backscatter signal strength using a gradient detection method. The top of a cloud is associated with a large increase in backscattered return and the presence of a cloud is determined by a much reduced (less than half the normal) surface return signal, due to the large attenuation of the laser beam by cumulus clouds. Cloud base height (for convective clouds) provides a good estimate of the height of the Lifting Condensation Level (LCL) (Stull and Eloranta, 1985). If the near-surface air temperature is also known, the near surface moisture can be calculated assuming that the air within the layer from the surface to the LCL is well mixed. While this is not always the case, it is a good assumption over open water, well removed from coastlines where upwelling of cooler water may induce a slightly stable atmospheric environment. The near-surface air temperature is estimated from the SST measurements. We assume that the near-surface air temperature is 0.8 C less than the radiometric sea surface temperature as measured by the SSTR. This assumption is generally very valid over the open ocean in the tropics and sub-tropics. Other investigations have found sea-air temperature differences of about 1 to 2 degrees Celsius with an average of about 1.5 degrees to be common over the tropical ocean. Weller and Anderson (1996) present measurements from two research ships and a moored buoy deployed in the center of the warm pool area as part of the TOGA COARE Intensive Flux Array (IFA). They found that the sea-air temperature difference was positive 98 percent of the time and varied between 1 and 2 degrees Celsius. During periods of light winds, a strong diurnal variation of SST is seen which significantly increases the sea-air temperature difference. Variability in air temperature was greater than that for the SST and is caused mainly by convective downdrafts and their wakes. We used a slightly lower sea-air temperature difference because all of our observations were acquired at night and the 0.8 degree Celsius sea-air temperature difference agreed well with the measured values based on the SSTR derived SST and the 10 meter air temperature measured by the dropsondes.

Once the near-surface air temperature and height of the LCL are known, the near-surface mixing ratio can easily be computed assuming a well mixed layer from the surface to the LCL. Details of the method can be obtained in Palm et al. (1998). Figure 3 is a plot of the near surface moisture (mixing ratio at 10 meter altitude ( $q_{10}$ )) as obtained by this retrieval method versus the observed near-surface moisture as measured by collocated dropsonde. Also shown on the plot are the near-surface moisture values retrieved from the SSM/I. It should be noted that the SSM/I retrievals are inherently much coarser spatially (2 x 2.5 degrees) than the P-3B measurements. Additionally, the SSM/I measurement can be as much as 12 hours either before or after the P-3B retrievals. This notwithstanding, the SSM/I retrievals agree very well with the P-3B data. The rms error of the P-3B retrieved near-surface mixing ratio (with respect to the dropsonde values) is about 0.8 g/kg with negligible bias. The results indicate that the moisture retrieval technique works over a relatively large range of surface moisture and provides an accuracy which is comparable to or better than the methods currently in use employing SSM/I measured microwave radiances.

### 2.2.2 MABL Structure Measurements

After the raw lidar data are range corrected and normalized by the laser energy they are horizontally averaged according to the acquisition mode. For the days where only nadir pointing data were collected, the data are averaged to a 1 second temporal resolution which yields a horizontal resolution of about 120 meters. For the data acquired in the across-track scan mode, the nadir shots are stripped from the scan sequence and two are averaged producing a horizontal resolution of about 350 meters. An example of the backscatter data collected by LASAL is shown in figure 4 which shows about 100 km of data centered on dropsonde number 1 from September 11<sup>th</sup>. The image color corresponds to relative backscatter signal strength where the largest signals are white, with signal strength decreasing through purple, green, light blue and dark blue. The potential temperature and water vapor mixing ratio are plotted on top of the image at roughly the position of the dropsonde launch. Also plotted on the image is the MABL height as determined by the gradient detection algorithm (black dotted line). The MABL height varies between about 500 and 600 meters in this image and is typical of the MABL height and structure encountered over the Atlantic.

The instantaneous boundary layer height ( $h$ ) is found for each averaged lidar profile using a gradient detection algorithm. The entrainment zone depth is calculated directly from the MABL heights using 50 km long segments by finding that height where 95 percent of the heights are below ( $h_1$ , the entrainment zone top) and that height where 95 percent of the heights are above ( $h_0$ , the entrainment zone bottom). The entrainment zone depth is defined as  $\Delta h = h_1 - h_0$ . This definition of the entrainment zone is similar to that used by Deardorff et al. (1980) and Melfi et al. (1985). The average boundary layer height for the segment ( $\bar{h}$ ) is calculated as the height where 50 percent of the MABL heights are above and 50 percent below. The standard deviation of the MABL top ( $\sigma(h)$ ) is computed from the instantaneous MABL height for the 50 km segment. The integrated backscatter signal through the depth of the boundary layer ( $S_i$ ) is defined as the average integrated relative backscatter signal from the MABL top to just above the surface averaged over the entire segment. These and other parameters have been calculated from the LASAL data at various locations along the flight track of the P-3B for all 5 LITE under flights based on 40 to 60 km long data segments. In section 4, we will investigate the relationship of the MABL structure parameters to the derived surface latent heat flux computed in the next section.

### 3. Flux Computation

In this section we combine the microwave scatterometer surface wind measurements and the LASAL-SSTR derived near surface moisture measurements to obtain estimates of latent heat flux for various points along the flight tracks shown in figure 1. The latent fluxes are then compared to the SSM/I daily fluxes interpolated to the same location. The ROWS wind speed is used in the computation of the fluxes except for 3 points where ROWS data were not available, in which case the CSCAT/KUSCAT winds are used instead. The scatterometer measurements have a horizontal resolution of about 1 km and about 50 km of wind data are averaged to obtain the wind speed magnitude used in the bulk flux computation. We will first examine the fluxes computed at the dropsonde locations and then add additional retrievals for areas in between the dropsonde points.

The only way to obtain a direct measurement of the turbulent fluxes of sensible heat and moisture is to measure the fluctuating quantities of temperature, moisture and wind for a considerable length of time (eddy correlation method). Since it is generally very difficult to obtain the necessary data, the turbulent fluxes are usually estimated using the bulk aerodynamic formulae, which relate the surface fluxes to gradients of wind ( $U$ ), moisture ( $q$ ) and temperature ( $\theta$ ) as follows:

$$H_s = \rho C_p C_H (U_z - U_s)(\theta_s - \theta_z) \quad (1a)$$

$$E_s = \rho L_v C_E (U_z - U_s)(q_s - q_z) \quad (1b)$$

where  $H_s$  and  $E_s$  are the sensible and latent surface heat flux, respectively,  $\rho$  and  $C_p$  the density and specific heat of dry air, respectively,  $L_v$  the latent heat of vaporization, and  $C_H$  and  $C_E$  are the transfer coefficients for heat and moisture, respectively. The reference height ( $z$ ) is usually taken to be 10 meters, and the subscript ( $s$ ) refers to the value of the variables at the sea surface. The wind at the surface ( $U_s$ ) is taken to be zero and the moisture at the surface ( $q_s$ ) is assumed to be the saturated value at the sea surface temperature. The transfer coefficients are a function of reference height, wind speed and atmospheric stability. Most of the difference among the various implementations of the bulk aerodynamic equations, is in the formulation of the transfer coefficients. Blanc (1985) reported that the average difference in transfer coefficients used in the ten bulk schemes he tested was 15-30 percent. Blanc's results indicated a need to test various formulations of the transfer coefficients against simultaneous direct measurements of the turbulent flux by eddy correlation. Chou (1993) compared four bulk schemes to a direct measurement of the flux by eddy correlation using airborne gustprobe measurements during the Mesoscale Air-Sea Exchange (MASEX) experiment. They found that on average, the bulk schemes agreed well with the eddy correlation method, but that the algorithm based on the flux profile relations of Francey and Garratt (1981) agreed best with the eddy correlation method.

Recently, methods have been developed by Chou et al. (1995, and 1997) to compute global fluxes over the oceans using the near surface moisture and wind retrievals from the Special Sensor Microwave Imager (SSM/I). The fluxes of heat, moisture, and momentum based on SSM/I data have been computed for a multi-year time period. This data set provides the only measurement of surface flux available over the oceans and is certainly better than could be computed from standard meteorological analysis such as the gridded ECMWF moisture, temperature and wind fields. The SSM/I fluxes are computed using the stability-dependent FG (Francey and Garratt, 1981) bulk scheme of Chou (1993). The bulk transfer coefficients are also dependent on wind speed and sea-air temperature and humidity differences. For the computation of bulk fluxes from the P-3B data in this paper, we have chosen to use the Chou algorithm to be consistent with the method used to produce the SSM/I fluxes, with which the P-3B fluxes will be compared.

Using the 10 meter wind speed retrievals of the microwave scatterometers, the measured SST and the lidar-radiometer retrieval of near surface moisture, we have employed equation 1b to compute the latent heat flux at various locations along the P-3B flight path for 4 of the 5 days. Flux computations were not possible for the September 17<sup>th</sup> under flight because for most of the flight there was a complete lack of cumulus clouds at the MABL top that made it impossible to compute the LCL which is needed to retrieve the near-surface moisture. Figure 5 shows the P-3B latent heat flux ( $W/m^2$ ) computed from the Chou algorithm plotted against the SSM/I daily average value. The SSM/I latent heat flux for a given P-3B location is obtained from the gridded (2.0 by 2.5 degree) SSM/I data by a  $1/d^2$  weighting of the nearest 4 SSM/I grid point values, where  $d$  is the distance from the SSM/I grid point to the P-3B location. The SSM/I data are from two separate satellites (F10, F11) and the x axis is an average of the F10 and F11 data. With the exception of a few outlying points, the latent heat flux computed from the combined lidar, radiometer and scatterometer data agrees fairly well with the SSM/I values but are

somewhat lower on average than the P-3B retrievals. The bias ( $P-3B - SSM/I$ ) is  $14.5 \text{ Wm}^{-2}$  and the rms difference is about  $40 \text{ Wm}^{-2}$ . Much of this difference is undoubtedly due to the lack of good temporal and spatial coincidence. The SSM/I data represent a spatial average over a box roughly  $200 \times 250 \text{ km}$  and can be as much as 12 hours apart in time from the P-3B measurements.

As noted above, the P-3B fluxes are biased high with respect to the SSM/I values. From equation 1b, we see that differences in latent heat flux arise from either the 10 meter wind speed or from differences in the values of the near-surface moisture gradient. Referring to figure 3, it can be seen that the 10 meter moisture retrieved from SSM/I agrees very well with the LASAL-radiometer retrieval at the dropsonde locations. Figure 6, which is a plot of the P-3B near-surface moisture retrievals versus the SSM/I value for all days also indicates that there is generally little difference between the SSM/I and P-3B near-surface moisture estimates. Further, the value of the saturated mixing ratio ( $q_s$ ) used in equation 1b is determined solely by the sea surface temperature. The surface saturated mixing ratio used in the SSM/I latent heat flux calculation is based on the NCEP (National Center for Environmental Prediction) weekly SST analysis. The surface saturated mixing ratio used for the P-3B latent heat flux estimate is based on the SSTR measured sea surface temperature. From the comparison shown in figure 2, it is seen that the NCEP sea surface temperature agrees very well with the SSTR measured value for the 16 dropsonde locations. These facts suggest that there should be little difference in the low-level moisture gradient ( $q_s - q_{10}$ ) at those points and we conclude that wind speed differences account for most of the difference in flux. In figure 7, we have plotted the SSM/I 10 meter wind speed versus the 10 meter wind speed retrieved from the microwave scatterometers onboard the NASA P-3B aircraft. With the exception of the points from 9/13 and 9/15, the SSM/I wind speeds are all considerably less than the scatterometer derived wind speed. It is not surprising that some of the SSM/I wind speeds are quite different from the P-3B measured winds since they represent a daily average over a  $2.0$  by  $2.5$  degree area. The P-3B measurement is a  $50 \text{ km}$  average of the wind centered at the dropsonde point and obtained at a time which may be considerably different than the time of the SSM/I measurement. Of the 3 variables that determine surface latent flux (SST, wind speed and 10 meter moisture), the wind field is likely to be the most variable, both temporally and spatially. It is therefore not surprising to see quite a bit of difference in the wind comparison, which directly contributes to the differences seen in the latent heat flux comparisons.

In the next section, the surface moisture fluxes for each day will be used to investigate their possible correlation with the various MABL structure parameters that were described in section 2. For the September 17<sup>th</sup> flight, we will use wind speed instead of flux for the correlation analysis, since fluxes are not available for that day. There are reasons to believe that MABL height, entrainment zone depth, variance of the MABL top and the integrated backscatter are related to the magnitude of the surface flux. We will discuss these reasons further in section 4 below.

#### **4. Correlation of MABL Structure with Surface Latent Heat Flux**

We used the P-3B latent heat flux data computed in section 3 at various locations along the flight path of the P-3B to investigate the possibility of correlation between the surface flux and the lidar-derived boundary layer parameters discussed above. There were on average about 15 to 20 latent heat flux retrievals for each flight day, except for September 17<sup>th</sup>, where the lack of a cumulus-capped MABL rendered it impossible to retrieve the LCL and thus the near surface moisture from the data. On this day,

we have used the wind speed instead of the flux for the correlation analysis. Since the surface flux is linear with wind speed, this seems like a reasonable thing to do.

It should be noted that in the following discussion the effect of  $\Delta\theta$  - that is the strength of the capping inversion at the MABL top - has been neglected. It will in practice have a large effect on entrainment zone depth and MABL height for a given surface flux. The same is true for the average large scale vertical velocity ( $\bar{w}$ ). While  $\Delta\theta$  is available from the dropsondes and  $\bar{w}$  can be estimated from ECMWF analysis, they will not be used here and we assume a constant temperature jump at the MABL top and a zero large scale vertical velocity. The main reason for this is that in many situations, these measurements will not be available over the oceans. One of the goals of this research is to use the methods developed here with the new orbiting lidar systems such as GLAS and PICASSO to obtain estimates of surface flux directly from the lidar data or from lidar data in combination with orbiting scatterometer instruments. In these applications, knowledge of  $\Delta\theta$  and  $\bar{w}$  will be tentative at best.

#### 4.1 MABL Height

In this section we investigate the possible links between surface latent heat flux and the height of the MABL as detected by lidar. The height of a convectively driven boundary layer is controlled by the entrainment rate and the synoptic scale vertical motion field. The equation governing the total rate of change of boundary layer depth ( $h$ ) with time is:

$$\frac{dh}{dt} = w_e + \bar{w} \quad (2)$$

Where  $w_e$  is the entrainment rate and  $\bar{w}$  is the large scale vertical motion (positive upwards). The entrainment rate is a function of the surface heat flux and can be expressed as:

$$w_e = \frac{A_R F_s}{\Delta\theta} \quad (3)$$

Where  $\Delta\theta$  is the average temperature jump across the inversion at the top of the boundary layer,  $F_s$  the surface heat flux and  $A_R$  is defined as  $F_h / F_s$  which is the ratio of the heat flux at the MABL top to the heat flux at the surface (Stull, 1988). For the case of free convection, the turbulence causing entrainment is directly related to the heat flux at the surface. This causes the flux at the top of the boundary layer to be nearly a constant fraction of the flux at the bottom (Ball, 1960). Most suggested values of  $A_R$  range between 0.1 to 0.3, with 0.2 the most frequently accepted value. Neglecting advection, the local rate of change of boundary layer height with time can be written as:

$$\frac{\partial h}{\partial t} = \frac{A_R F_s}{\Delta\theta} + \bar{w} \quad (4)$$

This equation implies that the total (sensible plus latent) heat flux at the surface partially governs the height of the boundary layer at any given time. Since, over the tropical and sub-tropical oceans, the

latent heat flux is generally about an order of magnitude larger than the sensible flux, we can use the latent heat flux ( $E_s$ ) as an estimate of the total flux.

A striking example of how MABL structure might be correlated with the surface flux can be gleaned from inspection of figure 8. This shows a portion of the flight from Cape Town South Africa to Ascension Island on September 17<sup>th</sup>, 1994 (flight 4). The lower panel is a color-coded rendition of the LASAL measured relative backscatter signal as a function of height and distance along the flight path. The largest signals are white, with signal strength decreasing through purple, green, light blue and dark blue. On the upper panel are plotted the ROWS derived 10 meter wind speeds which were measured simultaneously with the lidar backscatter. Speaking in general terms, the MABL is expected to be a layer of increased aerosol backscatter, since more aerosol and moisture are trapped there compared to the free atmosphere aloft. Thus, there is almost always an increase in lidar measured backscatter (gradient) at the MABL top. Referring to figure 8, at first glance one might think that the MABL top might be that layer which varies between about 800 m and 1 km. This is an erroneous interpretation, however. The true MABL top is the lower layer that starts out about 200 m thick and all but vanishes at about 150 km along the flight track. From that point it gradually grows to about 1 km at 800 km along the flight track. We know this to be true because of the thermodynamic sounding shown in figure 9, which was taken at about 200 km along the flight track. The profiles of moisture and temperature show a definite very shallow well mixed layer that is less than 100 m thick. An inversion at the top of the layer in both moisture and potential temperature indicate that this is a distinct layer independent from the deeper layer that extends up to about 1 km. The sounding in figure 9 was taken roughly 100 km west of the coast of South Africa. The wind direction in the lower 1 km of the atmosphere was generally east to west. This fact, together with the structure of the sounding between 200 and 900 m, indicates that the layer which extends up to 900 m to 1 km is in fact a continental boundary layer which has advected over the ocean.

The connection between the height of this lowest layer (the MABL) and the ROWS wind speed is obvious. The minimum in wind speed occurs at roughly the same time as the minimum in MABL height (between 150 and 200 km along the flight track). From that point the MABL steadily grows in depth as the wind speed increases. Given that the surface flux (as computed from bulk formulae) increases linearly with wind speed, it is natural to suppose a connection between the surface flux and the MABL height for the data presented in figure 8. Of course there are factors that could cause the low MABL height other than the magnitude of the surface flux. The most important factor is the synoptic scale vertical velocity. Inspection of the ECMWF surface pressure analysis shows that the minimum in wind speed and MABL depth measured by the ROWS and LASAL coincided with the crossing of a subtropical high pressure ridge. One might expect that the vertical velocity would be positive (sinking motion) in this area and also that its magnitude would be highest along the pressure ridge. We looked for this feature in the ECMWF analysis of vertical velocity, but it was not apparent. However, given the fact that this is a very data sparse region of the world and the fact that the resolution of the ECMWF analysis is much coarser than the P-3B measurements, it is conceivable that the ECMWF analysis was not able to resolve what was probably an area of strong sinking motion.

The strong relationship between MABL depth and the wind speed (and most probably flux) seen in figure 8 is quite intriguing. Might this type of behavior hold for other areas over the ocean as well? If so, then the surface latent heat flux should also be correlated with MABL height. To investigate this possibility, we computed the average height of the MABL at the location of the flux retrievals for the 5

days of the LITE under flights and correlated them with the P-3B derived surface latent heat flux (and with 10 meter wind speed for September 17<sup>th</sup>). Remember from section 2.2.1, that about 50 km of lidar data are used to derive the LCL which is then used in combination with the SST to derive the near-surface moisture. The mean MABL height plotted is computed from this same 50 km long segment. Figure 10 shows the surface latent heat flux (y axis) versus the average MABL depth for all data. Though there is quite a bit of scatter to the points, there is a definite trend indicating that higher surface flux is associated with increasing MABL depth. The correlation coefficient for the data in figure 10 is 0.39. However, the correlation coefficient for individual days is considerably higher. Tables 1 through 5 show the correlation of various MABL structure parameters with the P-3B (2<sup>nd</sup> column) and SSM/I derived latent heat flux and the scatterometer-derived 10 meter wind speed (except for Table 4, which shows correlation with the wind speed for September 17<sup>th</sup>). The data indicate a very high correlation between the surface flux and the mean MABL height for two of the five days (September 11<sup>th</sup> and 19<sup>th</sup>), and relatively high correlation for the other days. The highest correlation (0.97) occurs for the data from September 19<sup>th</sup>, but the lowest correlation is still relatively high at 0.6. We have fitted a polynomial to the data in figure 10 which has the form:

$$E_s = 113 + 0.09\bar{h} + 1.6 \times 10^{-5}(\bar{h})^2 \quad (5)$$

where  $E_s$  is the surface latent heat flux ( $\text{Wm}^{-2}$ ) and  $\bar{h}$  is the average MABL height in meters. This relationship obviously does not apply for shallow MABLs below about 200 m and indicates that the relationship is not linear as the MABL depth becomes small. This is seen in figure 11 which is a plot of the surface wind speed as a function of MABL height for September 17<sup>th</sup>. Readily apparent is the fact that for shallow MABL depth less than about 300 m, the relationship between wind speed and MABL depth is non linear, while it seems to be close to linear for larger MABL heights. In figure 11 we have fitted a 3<sup>rd</sup> order polynomial to the data which shows this non linear behavior at low MABL depth. The equation for the solid line is:

$$U = 1.71 + 0.018\bar{h} - 2.0 \times 10^{-5}(\bar{h})^2 + 6.9 \times 10^{-9}(\bar{h})^3 \quad (6)$$

where  $U$  is the 10 meter wind speed in  $\text{ms}^{-1}$ . Figure 11 also shows the 3<sup>rd</sup> order best fit (dotted) line of as a function of wind speed. The equation of the dotted line has the form:

$$\bar{h} = -246 + 312U - 89U^2 + 8.9U^3 \quad (7)$$

Obviously, equation 7 breaks down as the wind speed approaches zero. While there is a very striking correlation of wind speed and MABL height for the data from September 17<sup>th</sup>, and to a lesser extent for the 11<sup>th</sup>, 13<sup>th</sup> and 15<sup>th</sup>, this relationship does not hold for the data of September 19<sup>th</sup>. For this day, the surface wind speed was negatively correlated with all of the MABL structure parameters. The interesting thing about the 19<sup>th</sup> is that even with a negative correlation between MABL height and wind speed, the correlation between MABL height and latent heat flux was 0.97. This means that the wind speed did not drive the increase in surface flux as MABL height increased, but rather a large increase in the surface moisture gradient ( $q_s - q_{10}$ ) was responsible for the higher flux. This is shown in figure 12, where we have plotted the P-3B derived latent heat flux, the ROWS surface wind speed, MABL depth, and the near surface moisture gradient ( $q_s - q_{10}$ ) for the data from September 19<sup>th</sup>. The surface wind speed reaches a maximum at about 300 km and then gradually decreases by about 10 percent. During

this time, the near surface moisture gradient (the saturation value at the sea surface ( $q_s$ ) minus the value at 10 meters ( $q_{10}$ )) increases. The larger surface moisture gradient more than offsets the lower surface wind speed producing higher bulk fluxes. This is a very interesting result that is unique to the 19<sup>th</sup> and may be related to the flight track's proximity to the coast of Africa.

## 4.2 Entrainment Zone Depth

Boers and Eloranta (1986) noted that the depth of the entrainment zone for a convective mixed layer could be written as:

$$\Delta h = C \frac{\bar{\theta}_0 w_*^2}{g \Delta \theta} \quad (8)$$

where  $C$  is a constant,  $\bar{\theta}_0$  is the average potential temperature through the depth of the MABL,  $w_* = (g \bar{h} E_s / \bar{\theta}_0)^{1/3}$  is a turbulent vertical velocity scale which is a function of the average MABL height ( $\bar{h}$ ), and the surface latent heat flux ( $E_s$ ). This makes sense intuitively, as (8) implies that the entrainment zone depth is related to the magnitude of the surface flux and inversely to the strength of the capping inversion. Using lidar measured boundary layer height and entrainment zone depth of a daytime convective boundary layer over land, they found that the entrainment zone depth most closely followed the following equation:

$$\Delta h = C \left( \frac{\bar{\theta}_0 w_*^2}{g \Delta \theta} \right)^{0.41} \quad (9)$$

where  $C = 38.4$ . They note, however, that the fit was rather poor and indicate that other processes such as entrainment, gravity waves and wind shear at the boundary layer top play an important role in determining entrainment zone depth.

The entrainment zone depth was calculated from the LASAL data as discussed in section 2.2.2 and compared with the P-3B latent heat flux estimates for the same regions. The results are presented in figure 13. There is more scatter to the points than the plot of mean MABL depth versus flux and the correlation coefficient is lower at 0.27. Regardless, there is a tendency for high fluxes to correspond to deeper entrainment zones, though the relationship is rather weak. This seems to indicate that other factors such as the capping inversion strength or wind shear play important roles in determining entrainment zone depth. For most of the points in figure 13, we have no knowledge of the magnitude of  $\Delta \theta$ . However, at the dropsonde locations, this is easily obtained. At 14 of the 16 dropsonde locations we have computed the value of the right hand side of equation 9 and compared the result with the measured value of the entrainment zone depth ( $\Delta h$ ). The results are shown in figure 14, where the calculated value of  $\Delta h$  (y axis) is plotted versus the lidar measurement. The values calculated from equation 9 agree fairly well with the lidar measurements but do exhibit quite a bit of scatter.

Other investigators such Melfi et al. (1985) have suggested that the normalized entrainment zone depth ( $\Delta h/h_0$ ) is proportional to the entrainment rate for a convective boundary layer:

$$\Delta h / h_0 \cong 3(w_e / w_*)^{1/2} = 3(A_R E_s / (\Delta \theta w_*))^{1/2} \quad (10)$$

Equation 10 indicates that the latent flux at the surface is proportional to the normalized entrainment zone depth. In tables 1-5, we show the correlation of the normalized entrainment zone depth with the latent heat flux. The values are lower than for just the entrainment zone depth. This is mainly due to the relatively high correlation between  $h_0$  and the flux.

### 4.3 Integrated MABL Backscatter

In this section we define an integrated relative backscatter signal ( $S_i$ ) through the depth of the MABL and investigate its correlation with the surface latent heat flux.  $S_i$  is calculated by summing the relative backscatter return from just above the ocean surface (50 m) to the MABL top. The backscattered lidar signal received by LASAL is proportional to the atmospheric backscatter cross section and the two-way path transmission between the sampled region and the lidar. The computation of  $S_i$  will be affected by the attenuation caused by layers above the MABL. In general, this attenuation is effect is small, but when cumulus clouds are present at the MABL top, the attenuation is extremely large. In this case, the computed value of  $S_i$  will be invalid. Thus, we have identified and eliminated all data that were considered 'contaminated' by cumulus clouds. We determine the presence of clouds by searching for the ground return. When we cannot find a ground return signal, we assume that this is caused by the attenuating effects of a cloud. In general, this works well, but there will be times at the edges of clouds and over optically thin clouds where there will still be a surface return even though considerable attenuation of the lidar signal has occurred. In these cases, the integrated MABL backscatter signal will be less than it would have been in the absence of the cloud. We feel that the cloud screening accounts for most of the attenuating effects of clouds but acknowledge that attenuation due to clouds may have contaminated some of the  $S_i$  values.

The integrated relative backscatter signal through the depth of the MABL ( $S_i$ ) is dependent on MABL height and the magnitude of the atmospheric backscatter cross section profile through the depth of the MABL. The backscatter cross section is related to the aerosol number density and relative humidity profiles. The aerosols in the MABL are comprised mainly of sea salt, especially in areas far removed from continents, but can also contain a number of different aerosol types. The Aerosols99 experiment made in situ measurements of MABL aerosol properties during a ship cruise from Norfolk, Virginia to Cape Town, South Africa (Quinn et al., 2001). They measured significant quantities of sulfate ( $\text{SO}_4$ ), mineral dust and biomass burning in addition to the sea salt and nitrates that originate from the ocean. However, sea salt aerosol was the dominant component of the aerosol mass in all regions of the cruise with the exception of a small area dominated by Saharan dust (Bates et al., 2001). Given that the dominant source of aerosol in the MABL is the ocean, it makes sense to speculate that the amount of aerosol in the MABL will be dependent on the magnitude and sign of the exchange processes between ocean and atmosphere. The mechanism for the deposition of sea salt aerosol into the MABL is through agitation of the sea surface through wind force. Sea salt particles arise from the bursting of air bubbles when they reach the ocean surface. Bubbles are most numerous in the whitecaps associated with breaking waves. Whitecaps begin to appear at wind speeds of  $3\text{-}4 \text{ ms}^{-1}$  and cover about 1 percent of the ocean surface as the wind speed approaches  $8 \text{ ms}^{-1}$  (Warneck, 1988). Data from Blanchard and Woodcock (1980) indicate that sea salt concentration in the lower few hundred meters of the atmosphere increase by a factor of about 5 when surface wind speed increases from  $3$  to  $8 \text{ ms}^{-1}$ . During the LITE under flights, the wind speeds varied between about  $1$  and  $9 \text{ ms}^{-1}$ . Hence, there is good reason to believe

that the aerosol (sea salt component) loading of the MABL will contain variations induced by wind speed differences throughout the experiment area. These differences in aerosol loading should show up in the integrated MABL backscatter parameter ( $S_i$ ) and by inference should be related to the magnitude of the surface flux.

As mentioned above, for a given aerosol concentration, the relative humidity can affect the backscatter cross section. When the relative humidity exceeds about 80 percent, the hygroscopic aerosols (which includes sea salt) start to swell which increases their backscatter cross section. Thus, very moist MABL's would tend to have higher values of  $S_i$ . It may be possible that regions of relatively high surface moisture flux will result in MABLs with higher average relative humidity than areas of low surface moisture flux. If this is true, then the backscatter cross section, which is sensitive to relative humidity might also be higher. Thus there is further reason to believe that the integrated lidar received backscatter will be dependent on the magnitude of the surface flux.

Figure 15 shows the integrated backscatter amount plotted as a function of surface latent heat flux for 4 of the 5 under flights. On the 11<sup>th</sup> and 19<sup>th</sup>, the correlation is very high (0.87 and 0.95) while for the other 2 days, the correlation is about 0.5 (see tables 1 – 3, and 5). For all days, the correlation is about 0.7. It is clearly evident that the surface flux is related to the magnitude of the MABL integrated backscatter. It may be possible to derive a functional relationship between the integrated MABL backscatter and the surface heat flux which, when used in conjunction with measurements of MABL height, can give a good estimate of the surface heat flux over the ocean. To accomplish this, it would be necessary to compute calibrated, attenuation-corrected backscatter within the MABL. This would be especially important for an orbiting lidar, that would encounter many attenuating layers above the MABL.

## 5. Summary and Conclusions

We have demonstrated a way to obtain surface latent heat flux over the ocean using the combined measurements of airborne lidar, radiometer and microwave scatterometer. The lidar and radiometer data are used to derive an estimate of the 10 meter atmospheric moisture and the scatterometer retrieves the 10 meter wind speed. Of the 5 days for which data were acquired, 4 of them had sufficient scattered, broken clouds at the MABL top to estimate the height of the LCL and near-surface moisture. A bulk aerodynamic algorithm is then utilized to obtain the latent heat flux. The P-3B fluxes were computed for various points (65 in all) scattered over the tropical and sub-tropical Atlantic ocean and compared with the SSM/I daily average latent heat flux interpolated from a 2.0 x 2.5 degree grid to the same location. Results showed a positive bias (P-3B – SSM/I) of about 14 W/m<sup>2</sup> and an rms difference of about 40 W/m<sup>2</sup>. The later is in good agreement with the results of Jourdan and Gautier (1995) who compared in situ estimation of latent flux based on ship reports with SSM/I derived fluxes. Notable exceptions occurred in areas of the doldrums which were encountered by the P-3B in relatively small areas on September 15<sup>th</sup> and 17<sup>th</sup>. In these areas, the SSM/I wind speeds were considerably larger than those of the P-3B, causing the surface flux values to be greater as well.

The LASAL data were used to compute instantaneous MABL height for 40 – 60 km long segments at various points along the flight tracks shown in figure 1. From the MABL height data, other MABL parameters were computed such as average MABL height ( $\bar{h}$ ), entrainment zone top ( $h_1$ ), bottom ( $h_0$ ) and depth ( $\Delta h$ ), normalized entrainment zone depth ( $\Delta h / h_0$ ), the standard deviation of the MABL top ( $\sigma$ ),

and integrated backscatter signal within the MABL ( $S_i$ ). These parameters were then correlated with the surface latent heat flux to determine which, if any, had the highest relationship to the latent flux.

Boundary layer theory suggested that  $\bar{h}$ , and  $\Delta h$  should be related to the magnitude of the surface flux. Considerations regarding the mechanism of sea salt deposition into the MABL also argued for a relationship between the surface flux and  $S_i$ . We found that  $\bar{h}$ ,  $h_1$  and  $S_i$  were most highly correlated with the surface flux, with values of the correlation coefficient of 0.39, 0.43 and 0.71, respectively. The data from individual days exhibited considerably higher correlation often approaching or exceeding 0.9 for various MABL parameters. The entrainment zone depth ( $\Delta h$ ) and the standard deviation of the MABL top ( $\sigma(h)$ ) also showed high correlation with the heat flux and wind speed. Surprisingly, we found no correlation between normalized entrainment zone depth and latent heat flux because of the usually large positive correlation between  $h_0$  and the latent flux.

Most of the high flux correlation was due to a high correlation between the MABL parameters and wind speed. However, on September 19<sup>th</sup> we found that wind speed was negatively correlated with the MABL parameters, but yet high positive correlation was seen between the surface flux and MABL parameters. This was caused by a decrease in the value of the near-surface moisture as the wind speed decreased. The decreasing near-surface moisture increased the sea-air moisture gradient which more than compensated for the decreasing wind speed and caused an overall increase in the latent flux. The MABL structure parameters generally showed lower correlation with the SSM/I derived latent heat flux than for the P-3B derived fluxes for each day. However the SSM/I correlation for the data from all days was quite high for the entrainment zone depth, normalized entrainment zone depth and the standard deviation of the MABL top.

In future work we will include the effects of the temperature jump at the top of the MABL and the large scale vertical velocity in the analysis to determine their effect on the correlation of the surface latent heat flux with MABL height and especially normalized entrainment zone depth. Additionally, effort must be made to compute the calibrated backscatter within the MABL and attempt to correct for the attenuation of intervening layers if a generalized relationship between flux and/or windspeed and MABL backscatter is to be obtained. The ultimate goal of this work is to find a relationship between MABL parameters easily measured by lidar (such as those described in section 4) and the latent flux so that the later can be inferred from lidar measurements of MABL characteristics.

## 6. Acknowledgements

The authors wish to thank Dr. Sue Chou and Dr. Chung-Lin Shie for their gracious assistance in providing the SSM/I data and the FORTRAN code for computing the bulk fluxes. Denise Hagan of JPL provided the sea surface temperature measurements. Jay Donnelly and Jim Carswell of the University of Massachusetts collected and analyzed the KUSCAT scatterometer data. We also greatly appreciate the data analysis support provided by Ms. Kshama Bhattacharya and Mr. John Oduro.

## 7. References

Atlas, R., Hoffman, R. N., Bloom, S. C., Jusem, J. C. and Ardizzone, J.: 1996, "A Multiyear Global Surface Wind Velocity Dataset Using SSM/I Wind Observations." , *Bull. Amer. Meteor. Soc.*, **77**, 869-882.

- Atlas, R., Busalacchi, A. J., Ghil, M., Bloom, S. and Kalnay, E.: 1987, "Global surface wind and flux fields from model assimilation of SEASAT data", *J Geophys. Res. Oceans*, **92**, 6477-6487.
- Ball, F.K.: 1960, "Control of inversion height by surface heating", *Quart. J. Roy. Meteor. Soc.*, **86**, 483-494.
- Bates, T. S., Quinn, P. K., Coffman, D. J., Johnson, J. E., Miller, T. L., Covert, D. S., Wiedensohler, A., Leinert, S., Nowak, A. and Neus, C.: 2001, "Regional Physical and Chemical Properties of the Marine Boundary Layer Aerosol across the Atlantic during Aerosols99: An Overview", *J. Geophys. Res.*, Submitted
- Blanc, T.V.: 1985, "Variation of bulk-derived surface flux stability, and roughness results due to the use of different transfer coefficient schemes", *J. Phys. Oceanogr.*, **15**, 650-669.
- Blanchard, D. C. Woodcock, A. H.:1980, "The Production, Concentration and Vertical Distribution of the Sea-Salt Aerosol", *Ann. N.Y. Acad. Sci.* **338**, 330-347.
- Boers and Eloranta
- Chou, S.-H., Shie, C.-L., Atlas, R. M., Ardizzone, J. and Nelkin, E.: 2001, "A multiyear dataset of SSM/I-derived global ocean surface turbulent fluxes", *Bull. Amer. Meteor. Soc.*, (submitted).
- Chou, S.-H., Shie, C.-L., Atlas, R. M. and Ardizzone, J.: 1997, "Air-sea fluxes retrieved from special sensor microwave imager data", *J. Geophys. Res.*, **102**, 12,705-12,726.
- Chou, S-H., Atlas, R., C.-L Shie, C.-L. and Ardizzone, J.: 1995, "Estimates of surface humidity and latent heat fluxes over oceans from SSM/I data", *Mon. Wea. Rev.*, **103**, 2405-2425.
- Chou, S-H: 1993, "A comparison of airborne eddy correlation and bulk aerodynamic methods for ocean-air turbulent fluxes during cold-air outbreaks", *Boundary Layer Meteorol.*, **64**, 75-100.
- Dalu, G.: 1986, "Satellite remote sensing of atmospheric water vapor", *Int. J. Remote Sens.*, **7**, 1089-1097.
- Deardorff, J. W., Willis, G. E. and Stockton, B. H.: 1980, "Laboratory studies of the entrainment zone of a convectively mixed layer", *J. Fluid. Mech.*, **100**, 41-64.
- Francey, R. J. and Garratt, J. R.: 1981, "Interpretation of flux-profile observations at ITCE (1976)", *J. Appl. Meteor.*, **20**, 603-618.
- Hagan, D., Rogers, D., Friehe, C., Weller, R. and Walsh, E.: 1997: "Aircraft observations of sea surface temperature variability in the tropical pacific", *J. Geophys. Res.*, **102**, 15733-15747.
- Hagan, D.: 1988, "The profile of upwelling 11-micron radiance through the atmospheric boundary layer overlying the ocean", *J. Geophys. Res.*, **93**, 5294-5302.

- Hock, T. and Cole, H.: 1991, "A new aircraft universal lightweight digital dropsonde", *Seventh Symposium on Meteorological Observations and Instrumentation*, New Orleans, LA, Amer. Meteor. Soc., 291-296.
- Jourdan, D. and Gautier, C.: 1995, "Comparison between global latent heat flux computed from multisensor (SSM/I and AVHRR) and from in situ data", *J. Atmos. Oceanic Technol.*, **12**, 46-72.
- Kuo, Y. H. Reed, R. J. and Lownam, S.: 1991, "Effects of surface energy fluxes during the early development and rapid intensification stages of 7 explosive cyclones in the western Atlantic", *Mon. Wea. Rev.*, **119**, 457-476.
- Liu, W.T.: 1988, "Moisture and latent heat flux variabilities in the tropical Pacific derived from satellite data", *J. Geophys. Res.*, **93**, 6749-6760.
- McCormick, M. P.: 1996, "The flight of the Lidar In-space Technology Experiment (LITE)", *Advances in Atmospheric Remote Sensing with Lidar*, *Selected Papers of the 18<sup>th</sup> International Laser Radar Conference (ILRC)*, Albert Ansmann et al, Springer-Verlag, New York, New York, pp. 141-144.
- Melfi, S. H., Spinhirne, J., Chou, S.-H. and Palm, S. P.: 1985, "Lidar observations of vertically organized convection in the planetary boundary layer over the ocean", *J. Climate Appl. Meteor.*, **24**, 806-824.
- Palm, S. P., Hagan, D., Schwemmer, G and Melfi, S. H.: 1998, "Inference of marine atmospheric boundary layer moisture and temperature structure using airborne lidar and infrared radiometer data", *J. Appl. Meteor.*, **37**, 308-324.
- Palm, S. P., Melfi, S. H. and Carter, D. L.: 1994, "New airborne scanning lidar system: applications for atmospheric remote sensing", *Appl. Opt.* **33**, 5674-5681.
- Prabhakara, C., Dalu, G. and Kunde, V. G.: 1974, "Estimating of sea surface temperature from remote sensing in the 11 to 13  $\mu\text{m}$  window region", *J. Geophys. Res.*, **79**, 5039-5044.
- Quinn, P. K., Coffman, D. J., Bates, T. S., Miller, T. L., Johnson, J. E., Voss, K., Welton, E. J. and Neususs, C.: 2001, "Dominant Aerosol Chemical Components and Their Contribution to Extinction During the Aerosols99 Cruise across the Atlantic", *J. Geophys. Res.*, Submitted.
- Schulz, J. and Jost, V.: 2000, "A new satellite-derived freshwater flux climatology: The Hamburg ocean atmosphere parameters and fluxes from satellite data", *J. Climate*, (submitted).
- Spinhirne, J. and Palm, S. P.: 1997, "Space based atmospheric measurements by GLAS", *Advances in Atmospheric Remote Sensing with Lidar*, *Selected Papers of the 18<sup>th</sup> International Laser Radar Conference (ILRC)*, Albert Ansmann et al, Springer-Verlag, New York, New York, pp. 213-216.
- Stull, R.B.:1988, *An introduction to boundary layer meteorology*, Kluwer Academic Publishers, Boston, Massachusetts.

Stull, R. and Eloranta, E.: 1985: "A case study of the accuracy of routine, fair-weather cloud-base reports", *National Weather Digest*, **10**, 19-24.

Vandemark, D., Jackson, F., Walsh, E. and Chapron, B.: 1994, "Airborne radar measurements of ocean wave spectra and wind speed during the Grand Banks ERS-1 SAR wave experiment", *Atmos.-Ocean*, **32**, 143-178.

Warneck, P.: 1988, *Chemistry of the Natural Atmosphere*, Academic Press, Inc., San Diego, California, pp. 308-313.

Weller, R. A. and Anderson, S. P.: 1996, "Surface meteorology and air-sea fluxes in the western equatorial Pacific warm pool during the TOGA Coupled Ocean-Atmosphere Response Experiment", *J. Climate*, **9**, 1959-1990.

Winker, D. M. and Wielicki, A.: 1999, "The PICASSO-CENA Mission. in Sensors, Systems, and Next-Generation Satellites III", *Proceedings of SPIE*, **3870**, 26-36.

Zhang, G. J. and McPhaden, M. J.: 1995, "The relationship between sea surface temperature and latent heat flux in the equatorial Pacific", *J. Climate*, **8**, 589-605.

**Table 1.** Correlation of various MABL structure parameters and the P-3B and SSM/I derived latent heat flux, and the scatterometer derived surface wind speed, for the data acquired on September 11<sup>th</sup>, 1994.

MABL Parameter	P-3B Derived Flux Correlation	SSM/I Derived Flux Correlation	P-3B Wind Speed Correlation
$\sigma(h)$	0.79	0.49	0.51
$\bar{h}$	0.90	0.10	0.48
$h_0$	0.74	-0.21	0.38
$h_1$	0.83	0.21	0.51
$\Delta h$	0.61	0.34	0.45
$\Delta h/h_0$	0.20	0.42	0.06
$S_i$	0.87	0.25	0.23
$S_i/\bar{h}$	0.55	0.31	0.05

**Table 2.** Same as Table 1, except for September 13<sup>th</sup>.

MABL Parameter	P-3B Derived Flux Correlation	SSM/I Derived Flux Correlation	P-3B Wind Speed Correlation
$\sigma(h)$	0.47	-0.53	0.39
$\bar{h}$	0.78	0.12	0.76
$h_0$	0.40	0.39	0.54
$h_1$	0.81	-0.03	0.72
$\Delta h$	0.71	-0.24	0.53
$\Delta h/h_0$	0.24	-0.45	-0.01
$S_i$	0.46	-0.76	0.16
$S_i/\bar{h}$	0.21	-0.86	-0.11

**Table 3.** Same as Table 1, except for September 15<sup>th</sup>.

MABL Parameter	P-3B Derived Flux Correlation	SSM/I Derived Flux Correlation	P-3B Wind Speed Correlation
$\sigma(h)$	0.55	0.27	0.58
$\bar{h}$	0.65	0.20	0.61
$h_0$	0.21	-0.04	0.19
$h_1$	0.86	0.37	0.83
$\Delta h$	0.58	0.37	0.58
$\Delta h/h_0$	0.35	0.26	0.35
$S_i$	0.47	0.17	0.48
$S_i/\bar{h}$	0.29	0.15	0.32

**Table 4.** Correlation of various MABL structure parameters and the scatterometer derived surface wind speed, for the data acquired on September 17<sup>th</sup>, 1994.

MABL Parameter	P-3B Wind Speed Correlation
$\sigma(h)$	0.45
$\bar{h}$	0.68
$h_0$	0.71
$h_1$	0.65
$\Delta h$	0.41
$\Delta h/h_0$	-0.45

**Table 5.** Same as Table 1, except for September 19<sup>th</sup>.

MABL Parameter	P-3B Derived Flux Correlation	SSM/I Derived Flux Correlation	P-3B Wind Speed Correlation
$\sigma(h)$	0.40	-0.02	-0.34
$\bar{h}$	0.97	0.12	-0.15
$h_0$	0.95	0.13	-0.12
$h_1$	0.97	0.11	-0.17
$\Delta h$	0.37	-0.09	-0.30
$\Delta h/h_0$	-0.65	-0.19	-0.05
$S_i$	0.95	0.13	-0.16
$S_i/\bar{h}$	-0.25	0.07	-0.03

**Table 5.** Correlation of various MABL structure parameters and the P-3B and SSM/I derived latent heat flux, and the scatterometer derived surface wind speed, for all data acquired during the LITE under flights.

MABL Parameter	P-3B Derived Flux Correlation	SSM/I Derived Flux Correlation	P-3B Wind Speed Correlation
$\sigma(h)$	0.25	0.67	0.06
$\bar{h}$	0.39	0.10	-0.12
$h_0$	0.22	-0.34	-0.13
$h_1$	0.43	0.42	-0.08
$\Delta h$	0.27	0.74	0.02
$\Delta h/h_0$	0.20	0.72	0.08
$S_i$	0.71	-0.26	-0.10
$S_i/\bar{h}$	-0.10	-0.35	-0.08



## FIGURE CAPTIONS

**Figure 1.** Position of NASA-P-3B flight lines and dropsonde launches for the 5 under flights of the LITE experiment. The dropsonde launch positions are indicated by a '+' and are labeled by number (1-16).

**Figure 2.** The National Center for Environmental Prediction (NCEP) weekly analyzed sea surface temperature versus the SST as obtained from the SSTR measurements onboard the P-3B for the locations of the 16 dropsonde launches

**Figure 3.** The near-surface (10 meter) moisture obtained via the LASAL-radiometer retrieval method described in section 2.2.1 (•) and the SSM/I 10 meter moisture (x) compared to dropsonde measurements at the same location and time.

**Figure 4.** An example of the relative attenuated backscatter signal acquired by LASAL during the LITE under flights. The largest signal is indicated by white, with decreasing values through purple, green, and blue. The data are from the northernmost portion of the September 11<sup>th</sup> flight track and show the top of the MABL as the dotted line. Also plotted are the mixing ratio (left profile) and the potential temperature as measured by dropsonde.

**Figure 5.** The latent heat flux ( $W/m^2$ ) derived from the P-3B measurements versus the SSM/I average daily value interpolated to the P-3B location for all retrievals. The dark symbols are retrievals made at the dropsonde locations.

**Figure 6.** SSM/I derived near-surface moisture ( $q_{10}$ ) versus the P-3B retrieved value for all retrievals made for the 5 under flights..

**Figure 7.** A comparison of the average 10 meter wind speed derived from the P-3B scatterometers and the 10 meter wind speed retrieved from SSM/I for the same locations.

**Figure 8.** An image of the LASAL measured relative backscatter (lower panel) and the simultaneously measured ROWS 10 meter wind speed for the September 17<sup>th</sup> under flight. The increased backscatter at 800 m altitude is due to a continental layer which has been advected over the ocean from Africa. The MABL is the lower layer that ranges from less than 100 m to 1 km at the far right side of the image.

**Figure 9.** The mixing ratio (left curve) and potential temperature measured by a dropsonde that was launched at about the 200 km point (x axis) of figure 8.

**Figure 10.** A scatter plot of the average MABL depth and P-3B derived latent heat flux for all points. Also shown is the 2<sup>nd</sup> order polynomial best line fit through the data (equation 5).

**Figure 11.** A plot of the ROWS derived near surface wind speed versus the simultaneous LASAL measurement of the depth of the MABL for September 17<sup>th</sup>. Also shown are the third order polynomial fits of wind speed as a function of MABL depth (dotted line) and the MABL depth as a function of wind speed.

**Figure 12.** The P-3B derived surface latent heat flux, near surface wind speed, average MABL depth and near surface moisture gradient ( $q_s - q_{10}$ ) as a function of along-track distance for September 19<sup>th</sup>.

**Figure 13.** A scatter plot of the MABL entrainment zone thickness and the P-3B surface latent heat flux for all points.

**Figure 14.** The measured MABL entrainment zone depth versus the calculated value using equation 9 for the data at the dropsonde points.

**Figure 15.** A scatter plot of the integrated MABL backscatter and the P-3B surface latent heat flux for all points.

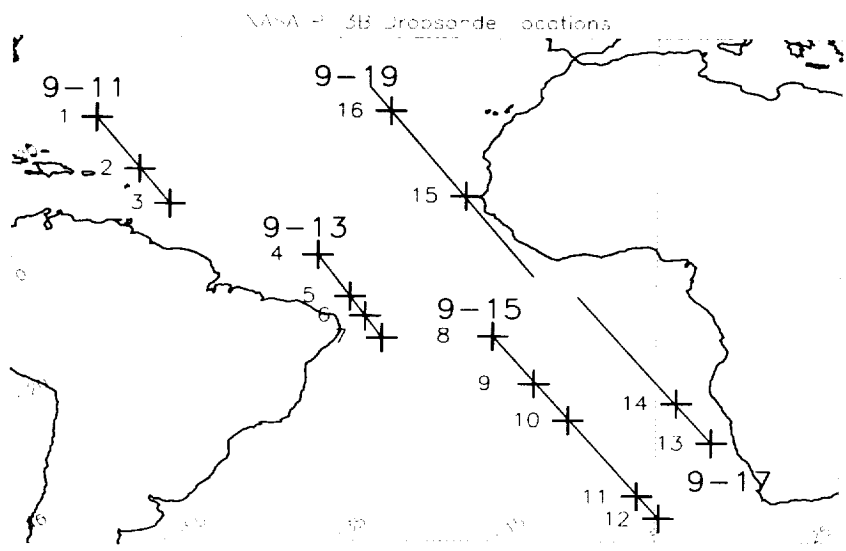


Fig 1

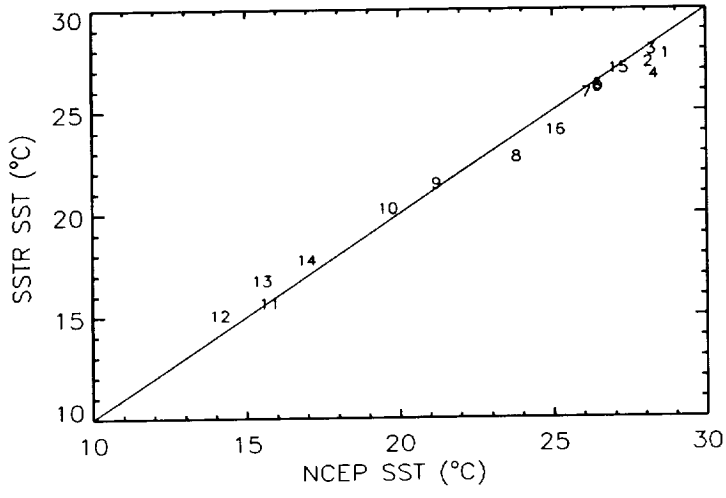


Fig 2

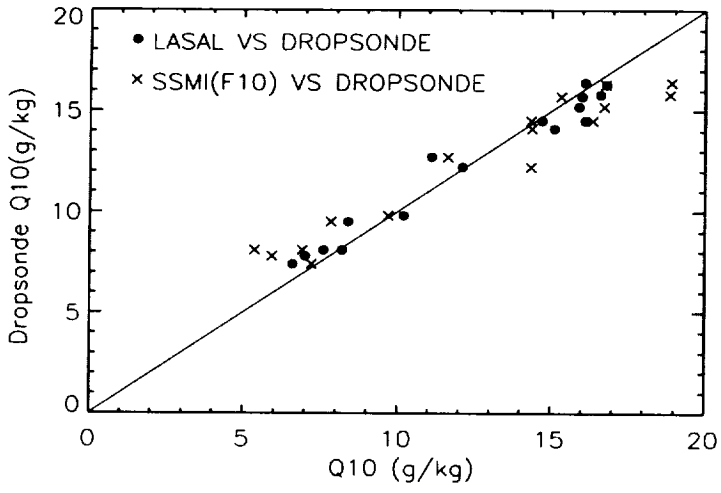


Fig 3

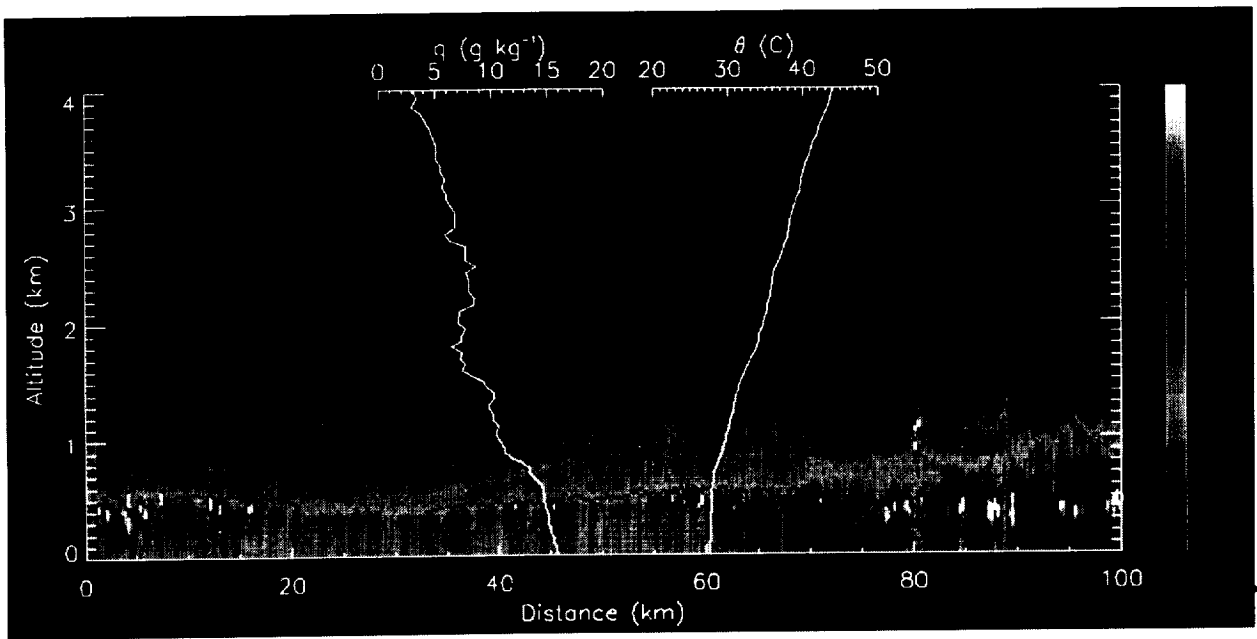
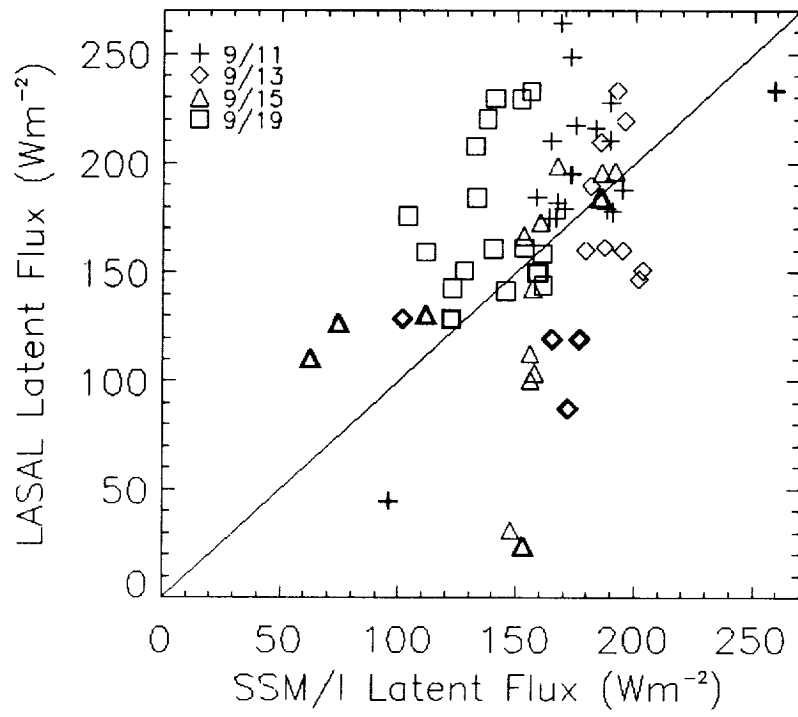


Fig 4

Fig 5



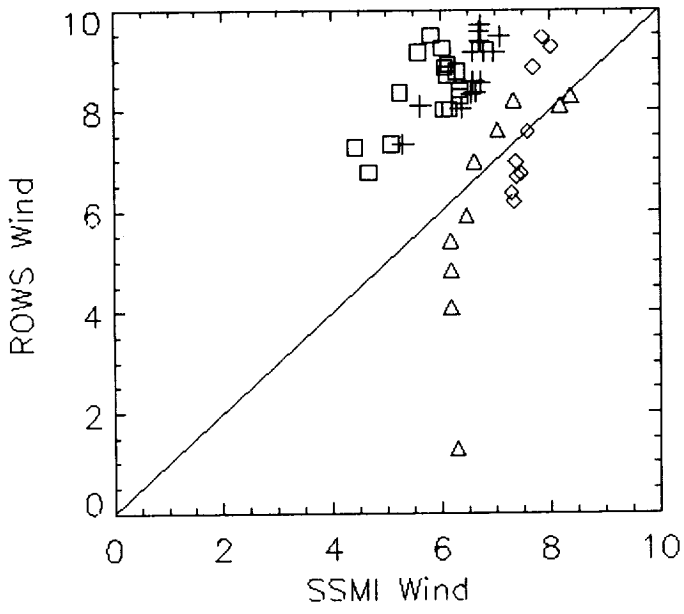


Fig 6

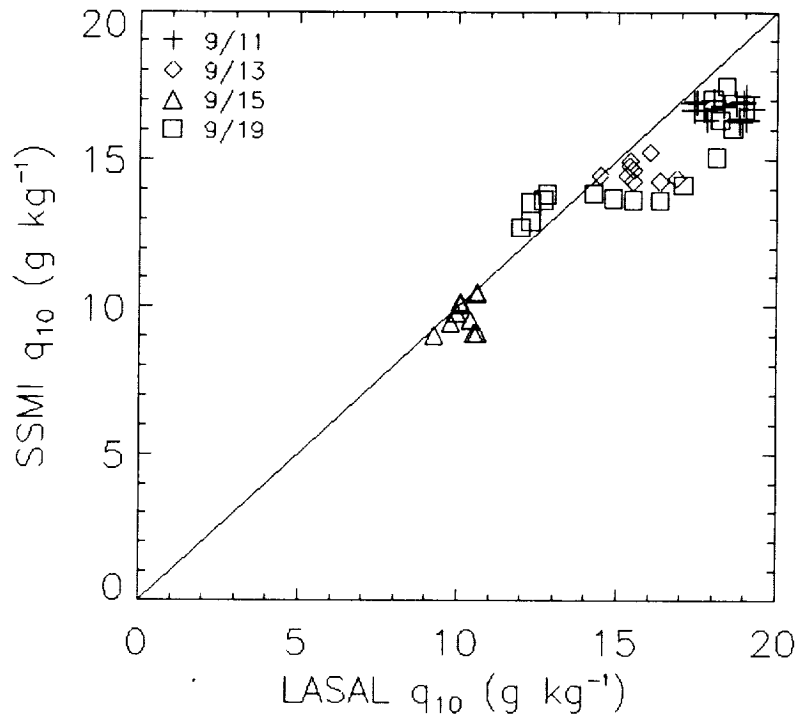


Fig 7

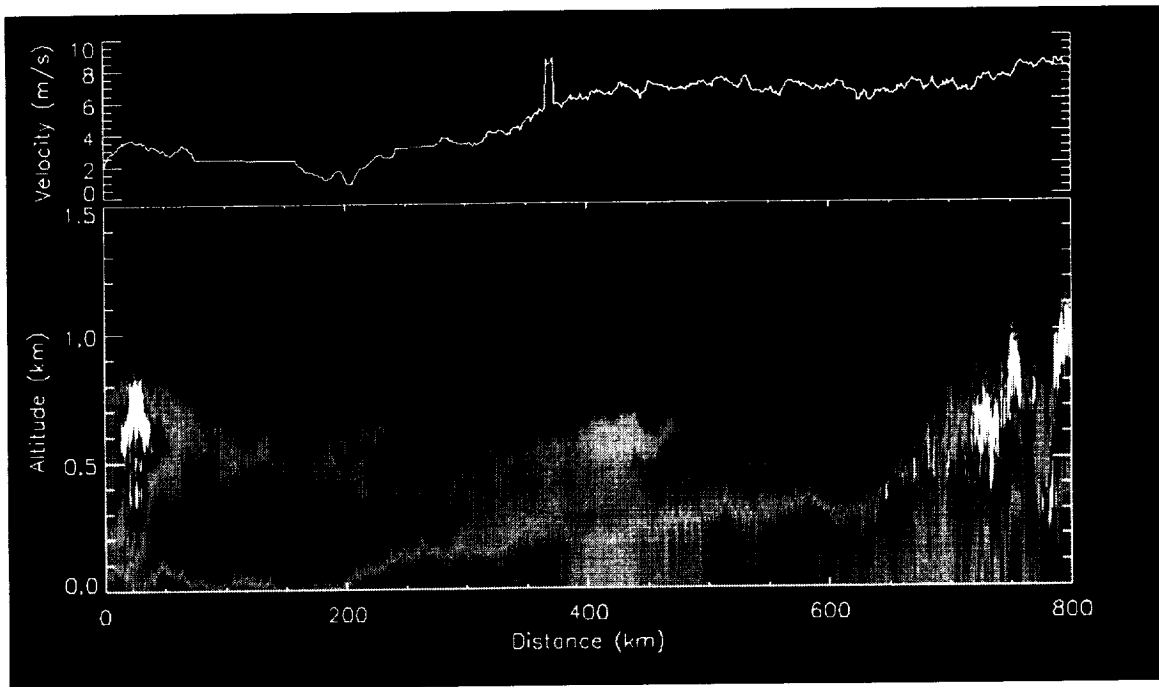


Fig 8

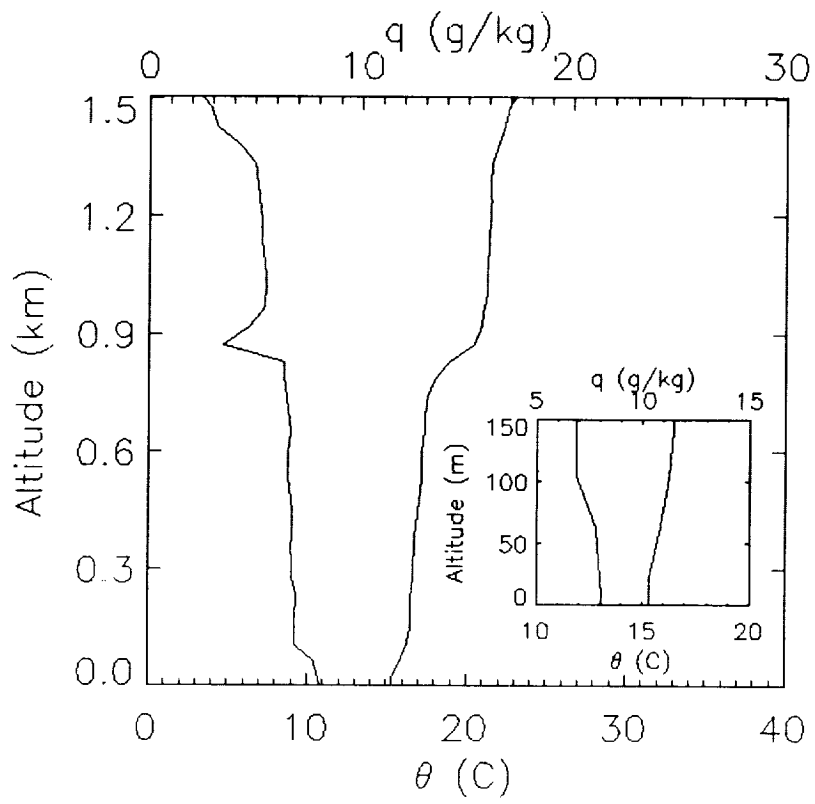


Fig 9

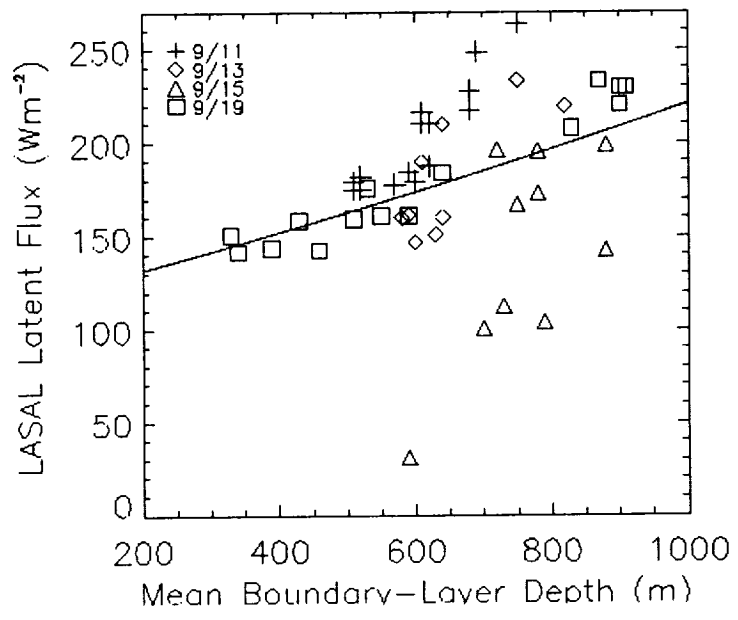


Fig 10

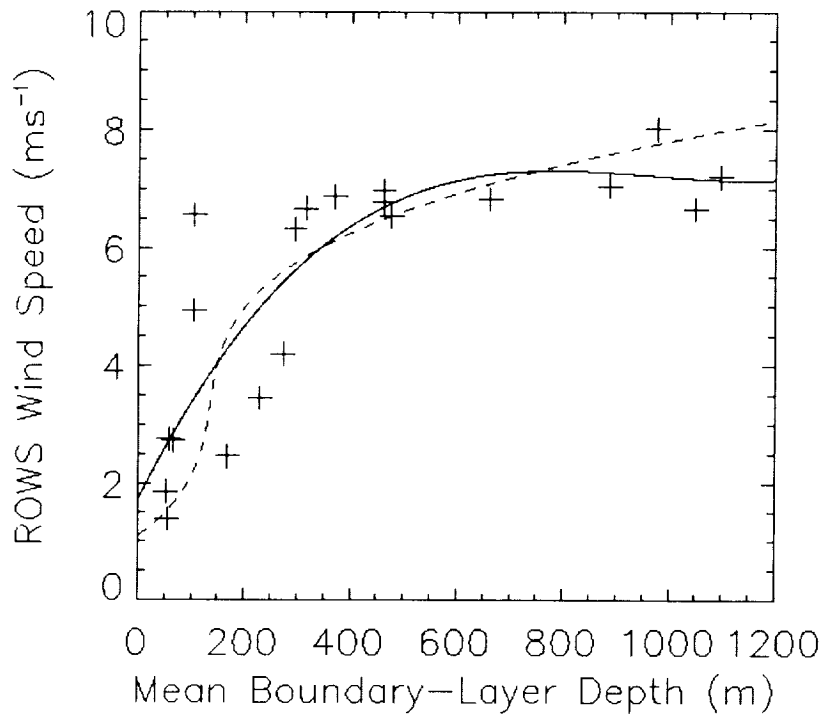
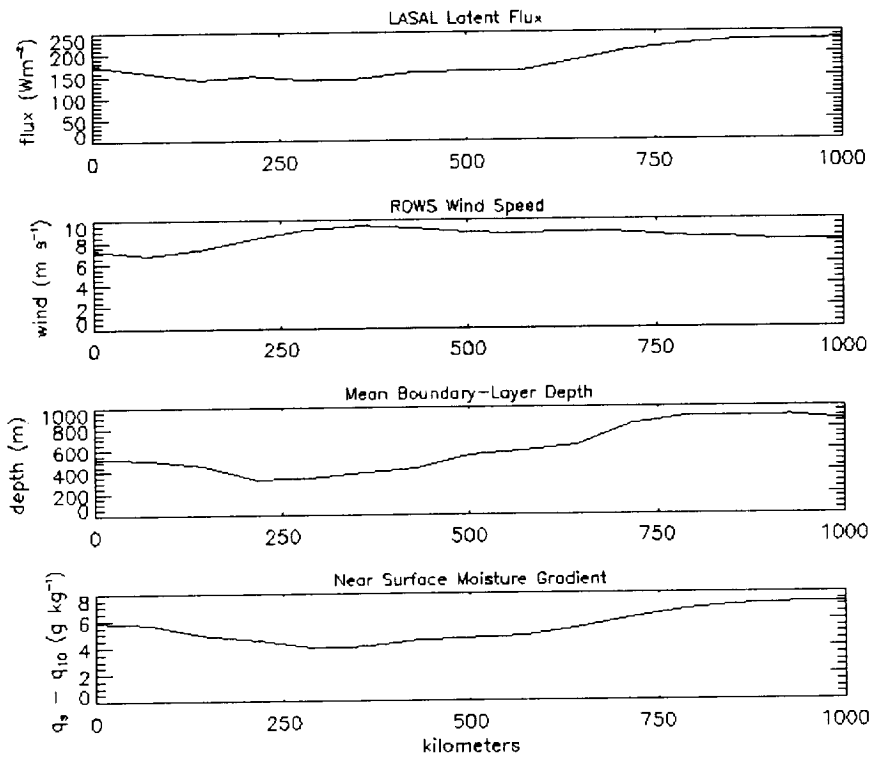


Fig 11

Fig 12



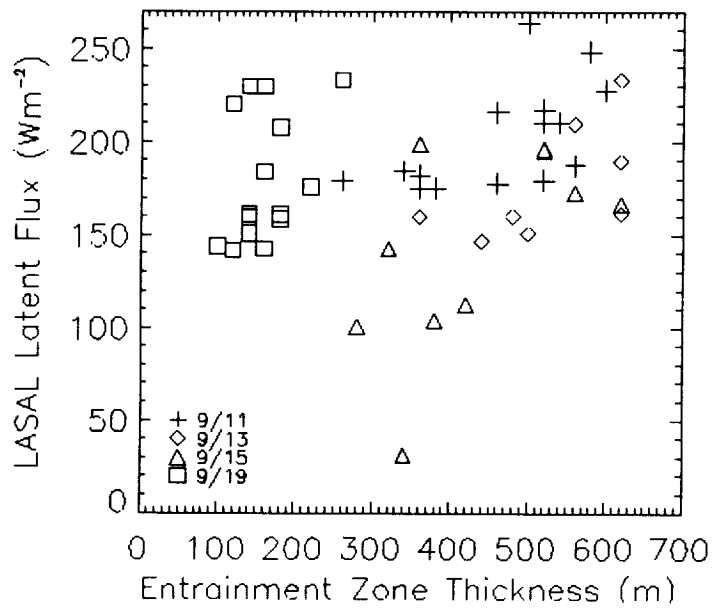


Fig 13

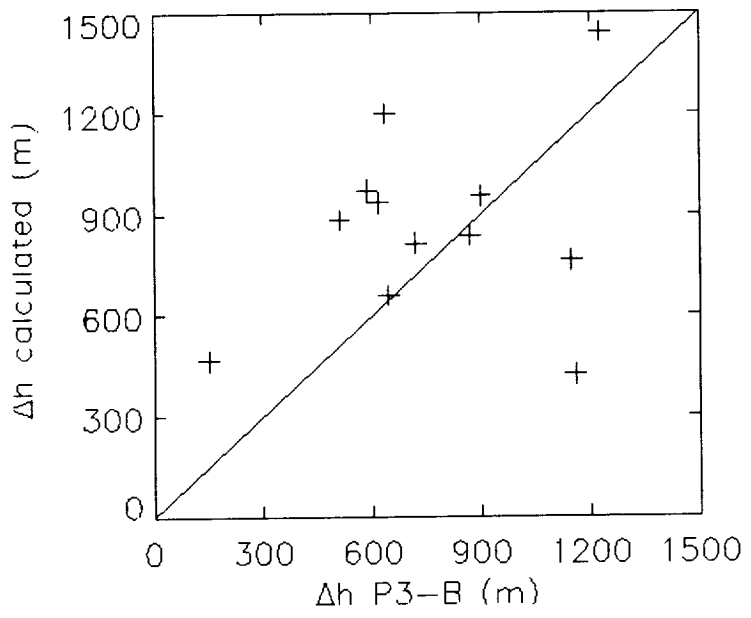


Fig 14

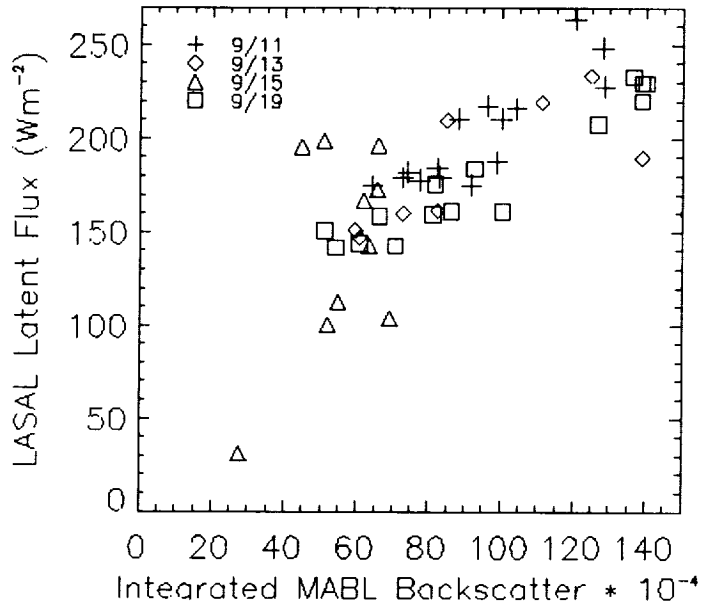


Fig 15